Electron Density Distribution of an Oxamato Bridged Mn(II)−Cu(II) Bimetallic Chain and Correlation to Magnetic Properties

Sébastien Pillet,[†] Mohamed Souhassou,[†] Corine Mathonière,[‡] and Claude Lecomte*,[†]

Contribution from the Laboratoire de Cristallographie et Modélisation des Matériaux Minéraux et Biologiques, Université Henri Poincaré, UMR CNRS 7036, 54506 Vandoeuvre les Nancy, France, and Laboratoire des Sciences Moléculaires, Institut de Chimie de la Matière Condensée de Bordeaux, UPR CNRS 9048, 33608 Pessac, France

Received May 6, 2003; E-mail: claude.lecomte@lcm3b.uhp-nancy.fr

Abstract: The electron density distribution of the ferrimagnetic MnCu(pba)(H$_2$O)$_3$·2H$_2$O chain compound, where pba stands for 1,3-propylenebis(oxamato), has been derived from high resolution X-ray diffraction measurements at 114 K using a multipolar model. The analysis of the chemical bonding has been carried out through the "Atoms in Molecules" formalism and thoroughly interpreted with regards to the strong intrachain and weak interchain magnetic couplings. The topological properties of the electron density on the oxamato bridge indicate large electron delocalization and conjugation effects, in addition to high charge transfer from both metals to the bridge. The resulting positive charges on Mn (+1.45 e) and Cu (+1.56 e) induce charge polarization of the bridge, leading to a shift of electron density from the central C atoms to the metal coordinating O and N atoms. The Mn-bridge interactions are mainly closed-shell interactions with low electron density at the corresponding bond critical points, whereas the Cu-bridge interactions exhibit significant covalent character. The Cu−N bonds are moreover stronger than the Cu−O bonds. The 3d Cu and Mn orbital populations are consistent with pyramidal and regular octahedral environments, respectively, in agreement with the loss of degeneracy due to ligand field effects. Interchain interaction pathways are evidenced by the existence of four bond critical points in hydrogen bond regions. Finally, these intrachain and interchain bonding features are correlated to the results of experimental and theoretical spin density distributions, as well as magnetic measurements.

Introduction

In the last two decades, molecular magnetism has been a very attractive and fruitful field of investigation,[1] dealing with the design of magnetic molecular entities using organic and organometallic building blocks. In this context, numerous systems have been synthesized revealing interesting magnetic properties, like room-temperature ferrimagnetism,[2,3] low dimensional properties,[4] and photoinduced magnetization.[5−10] Many studies have been devoted to polymetallic compounds,[11−21]

as several important concepts, based on molecular magnetic orbital overlap and symmetry considerations,[22−24] have been introduced to rationalize the magnetic couplings between metal centers. Ordered bimetallic chains, consisting of metal ions bridged by bis-bidentate ligands such as oxamato, oxalato,

† Université Henri Poincaré.
‡ Institut de Chimie de la Matière Condensée de Bordeaux.
(1) Kahn, O. *Molecular Magnetism*; VCH: New York, 1993.
(2) Ferlay, S.; Mallah, T.; Ouahès, R.; Veillet, P.; Verdaguer, M. *Nature* **1995**, *378*, 701.
(3) Mallah, T.; Thiebaut, S.; Verdaguer, M.; Veillet, P. *Science* **1993**, *262*, 1554.
(4) Laget, V.; Hornick, C.; Rabu, P.; Drillon, M.; Ziessel, R. *Coord. Chem. Rev.* **1998**, *178−180*, 1533.
(5) Sato, O.; Iyoda, T.; Fujishima, A.; Hashimoto, K. *Science* **1996**, *272*, 49.
(6) Verdaguer, M. *Science* **1996**, *272*, 698.
(7) Ohkoshi, S.; Machida, N.; Abe, Y.; Zhong, F. J.; Hashimoto, K. *Chem. Lett.* **2001**, 312.
(8) Bleuzen, A.; Lomenech, C.; Escax, V.; Villain, F.; Varret, F.; Cartier dit Moulin, C.; Verdaguer, M. *J. Am. Chem. Soc.* **2000**, *122*, 6648.
(9) Escax, V.; Bleuzen, A.; Cartier dit Moulin, C.; Goujon, A.; Varret, F.; Verdaguer, M. *J. Am. Chem. Soc.* **2001**, *123*, 12536.
(10) Shimamoto, N.; Ohkoshi, S.; Sato, O.; Hashimoto, K. *Inorg. Chem.* **2002**, *41*, 678.

(11) Baron, V.; Gillon, B.; Plantevin, O.; Cousson, A.; Mathonière, C.; Kahn, O.; Grand, A.; Orstrom, L.; Delley, B. *J. Am. Chem. Soc.* **1996**, *118*, 11824.
(12) Kahn, O.; Pei, Y.; Verdaguer, M.; Renard, J. P.; Sletten, J. *J. Am. Chem. Soc.* **1988**, *110*, 782.
(13) Gatteschi, D.; Guillou, O.; Zanchini, C.; Sessoli, R.; Kahn, O.; Verdaguer, M.; Pei, Y. *Inorg. Chem.* **1989**, *28*, 287.
(14) Nakatani, K.; Bergerat, P.; Codjovi, E.; Mathonière, C.; Pei, Y.; Kahn, O. *Inorg. Chem.* **1991**, *30*, 3977.
(15) Pei, Y.; Verdaguer, M.; Kahn, O.; Sletten, J.; Renard, J. P. *J. Am. Chem. Soc.* **1986**, *108*, 7428.
(16) Pei, Y.; Verdaguer, M.; Kahn, O.; Sletten, J.; Renard, J. P. *Inorg. Chem.* **1987**, *26*, 138.
(17) Baron, V.; Gillon, B.; Cousson, A.; Mathonière, C.; Kahn, O.; Grand, A.; Ohrstrom, L.; Delley, B.; Bonnet, M.; Boucherle, J. X. *J. Am. Chem. Soc.* **1997**, *119*, 3500.
(18) Kahn, O.; Mathonière, C.; Srinivasan, B.; Gillon, B.; Baron, V.; Grand, A.; Ohrstrom, L.; Ramasesha, S. *New J. Chem.* **1997**, *21*, 1037.
(19) Cador, O.; Mathonière, C.; Kahn, O. *Inorg. Chem.* **2000**, *39*, 3799.
(20) Champion, G.; Arrio, M. A.; Sainctavit, P.; Zacchigna, M.; Zangrando, M.; Finazzi, M.; Parmigiani, F.; Villain, F.; Mathonière, C.; Cartier dit Moulin, C. *Monatsh. Chem.* **2003**, *134*, 277.
(21) For review papers in magnetism, see: *Molecules to Materials I, II, III, IV*; Miller, J. S., Drillon, M., Eds.; VCH: New York, 2001 and 2002.
(22) Hay, P. J.; Thibeault, J. C.; Hoffmann, R. *J. Am. Chem. Soc.* **1975**, *97*, 4.
(23) Kahn, O.; Briat, B. *J. Chem. Soc., Faraday Trans. II* **1976**, *72*, 268.
(24) Kahn, O.; Briat, B. *J. Chem. Soc., Faraday Trans. II* **1976**, *72*, 1441.

oxamido, and thio-oxalato, have attracted much attention.[21] These compounds usually lead to mainly low dimensional ferromagnetic or antiferromagnetic interactions along the chains. Depending on the molecular structure and crystal packing, weak interchain couplings can moreover be superimposed, giving rise to three-dimensional interactions and sometimes magnetic ordering. Among these systems, infinite bimetallic $Mn^{II}-Cu^{II}$ chains have been the subject of several studies,[12−20] the high magnetic moment per (Mn^{II}−ligand−Cu^{II}) unit allowing intense couplings despite the high Mn−Cu separation along the chains.

This paper is devoted to the investigation of the electron density (ED) distribution of the bimetallic chain compound $MnCu(pba)(H_2O)_3\cdot2H_2O$, where pba stands for 1,3-propyl-enebis(oxamato), at 114 K. The crystal structure has been derived at room temperature by Pei et al.[16] from X-ray diffraction measurements and at 10 K by Baron et al.[17] from neutron diffraction techniques. It can be described as infinite parallel Mn−pba−Cu chains connected to each other by hydrogen bonds. Correlatively, $MnCu(pba)(H_2O)_3\cdot2H_2O$ exhibits a magnetic behavior typical of ordered bimetallic chains, with one-dimensional antiferromagnetic interactions ($J = -23.4$ cm^{-1}) and weak interchain couplings.[16] Its magnetic behavior has been further investigated from polarized neutron diffraction measurements using a spin density restricted multipolar model.[17] The negative and positive spin densities observed on Cu (-0.75-(2)μ_B) and Mn ($+4.93(3)\mu_B$) are characteristic of antiferromagnetic interactions along the chains. In addition, spin densities have been observed on the oxamato moiety with positive contributions on the O atoms connected to Mn and negative populations on all the other atoms. Baron et al.[17] have thus explained the magnetic interactions between Mn and Cu by a spin delocalization mechanism through the oxamato bridge. Contrary to what can be expected from the higher spin population on Mn, spin delocalization is more efficient on the copper side of the oxamato bridge. These effects have been confirmed on molecular fragments by theoretical DFT spin density calculations and on a simulated chain system using a density matrix renormalization group formalism.[18] These theoretical calculations point out also small spin polarization of the oxamato group. Cador et al.[19] performed optical absorption measurements of the Mn^{II} spin forbidden transitions and deduced a coupling J value in agreement with the magnetic measurements. An XMCD study[20] confirmed the Mn and Cu spin populations observed from PND techniques. Although the nature of the magnetic interactions and the mechanism involved seem to be well understood, several points concerning the bonding interactions need to be further clarified. The polarized neutron diffraction experiments give information on the atomic nature of the interactions through the atomic spin populations; the optical and magnetic measurements are on the other side restricted to a macroscopic point of view. The ED analysis is a powerful tool to study chemical bonding in solids.[25−27] Chemical and physical properties can be derived from the ED such as electrostatic potential, atomic charges, dipole moments, hydrogen bond kinetic and potential energy densities, and so forth.

We have shown in previous studies on radicals[28,29] and organometallic systems[30] that the ED analysis gives light on some aspects related to the magnetic interactions in molecular systems, like 3d atomic orbitals populations, atomic charges and charge transfer, electron polarization, and so forth. A complete description of the chemical bonding, including the spin component, arises from the comparison of experimental X-ray and polarized neutron diffraction results.[31−33] The ED analysis we report here goes beyond the present $MnCu(pba)(H_2O)_3\cdot2H_2O$ system and allows us to give some insights about chemical bonding in bimetallic chains in a more general point of view.

This paper is divided into four parts including the Introduction. We describe in part 2 the high-resolution X-ray data measurements and the multipolar model used to recover the ED distribution of the title compound. The results of ED analysis and the investigation of the intrachain and interchain chemical bonding are given in part 3. Part 4 is devoted to the interpretation of the properties deduced from the ED in terms of magnetic couplings.

Experimental Section

X-ray Diffraction Data Collection and Reduction. MnCu(pba)-$(H_2O)_3\cdot2H_2O$ was synthesized as previously reported,[16] giving light blue platelike samples. First X-ray diffraction tests showed that the crystal quality was limited, due to a layer crystal growing process. After many trials, a well shaped single crystal of dimensions $0.3 \times 0.3 \times 0.2$ mm^3, suited for a charge density study, was selected and mounted on a Nonius Kappa CCD diffractometer using graphite monochromatized Mo Kα radiation and equipped with an Oxford Cryosystem. To decrease thermal smearing effects, the sample was cooled to 114 K; the temperature was beforehand calibrated using the ADP para-electric to anti-ferroelectric phase transition at 148 K. X-ray diffraction data were collected using ω-scans at different θ detector positions ($2\theta = 0°$, $20°$, $22.4°$, and $24.3°$) to allow high redundancy and high-resolution data measurements. Oscillation width ($2°$) and exposure time (180 s) were selected and kept constant throughout the experiment to ensure a high consistency of the data set and to allow a high signal-to-noise ratio of each intensity peak, even for the high angle weak reflections, without saturating the detector for low order reflections. 48 889 reflections were integrated on 894 frames up to a resolution of 0.98 Å^{-1} with the DENZO program[34] implemented in the HKL2000 package. Final cell parameters were deduced from a least-squares postrefinement on all measured reflections. Interframe scaling using the intensity of equivalent reflections was checked and did not show any crystal decay during data collection; this scaling procedure was nevertheless applied. The crystal faces were indexed and accurately measured to correct from absorption effects by Gaussian integration (ABSORB[35]). Diffracted intensities were reduced and merged in the mmm Laue group, using program SORTAV,[36] yielding 4567 unique reflections of which 3301 have $I > 3\sigma(I)$. The internal agreement factor increases in a regular way versus resolution, from 3.3% at 0.5 Å^{-1} to less than 10% in the

(25) Coppens, P. *X-ray Charge Densities and Chemical Bonding*; IUCr, Oxford University Press: 1997.
(26) Lecomte, C.; Souhassou, M.; Pillet, S. *THEOCHEM* **2003**, *647*, 53.
(27) Lugan, N.; Ortin, Y.; Mathieu, R.; Lepetit, C.; Heullt, J. L.; Pillet, S.; Souhassou, M.; Jelsch, C.; Lecomte, C. *SFC Eurochem.* **2002**.

(28) Pillet, S.; Souhassou, M.; Pontillon, Y.; Caneschi, A.; Gatteschi, D.; Lecomte, C. *New J. Chem.* **2001**, *1*, 131.
(29) Claiser, N.; Souhassou, M.; Lecomte, C.; Pontillon, Y.; Romero, F.; Ziessel, R. *J. Phys. Chem.* **2002**, *106* (50), 12896.
(30) Pillet, S.; Souhassou, M.; Lecomte, C.; Rabu, P.; Massobrio, C.; Drillon, M. ECM 19, 2000, Abstract p 127.
(31) Becker, P.; Coppens, P. *Acta Crystallogr.* **1985**, *A41*, 177.
(32) Figgis, B. N.; Kucharski, E. S.; Reynolds, P. A. *Acta Crystallogr.* **1989**, *B45*, 240.
(33) Figgis, B. N.; Reynolds, P. A.; White, A. H. *J. Chem. Soc., Dalton Trans.* **1987**, 1737.
(34) Otwinowski, Z.; Minor, W. *Methods in Enzymology*, *276*; Carter, C. W., Jr., Sweet, R. M., Eds.; Academic Press: 1996.
(35) Detitta, G. T. *J. Appl. Crystallogr.* **1985**, *18*, 75.
(36) Blessing, R. H. *J. Appl. Cryst.* **1989**, *22*, 396.

Table 1. Crystallographic Data and Experimental Details

$$R_{int} = \frac{\sum_{H}\sum_{i=1}^{Neq}|I_i(H) - \langle I(H)\rangle|}{\sum_{H}\sum_{i=1}^{Neq}|I_i(H)|}$$

$a/b/c$ (Å)	12.7858(5)/21.2972(8)/5.1864(2)
V (Å³)/Z	1412.3(2)/4
space group/crystal system	*Pnma*/orthorhombic
temperature (K)/wavelength (Å)	114/Mo Kα 0.71073
scan method/rotation width (deg)	rotation $\omega/2$
exposure time per frame (s)	180
crystal to detector distance (mm)	40
no. of frames	894
data collection time (hours)	~90
refined mosaïcity (deg)	1.16
μ (mm⁻¹)/T_{min}/T_{max}	2.43/0.55/0.64
no. of measured/independent reflections	48889/4567
$(\sin\theta/\lambda)$ max (Å⁻¹)/ completeness (%)/redundancy	0.98/81.3/10.5
range of h/k/l	$-24 < h < 23/-38 < k$ $< 38/-9 < l < 9$
$R_{int}(I)$ (%), all data	3.60

Table 2. Agreement Indices for the Two Refinement Models $(0 < (\sin(\theta)/\lambda) < 0.98$ Å⁻¹)

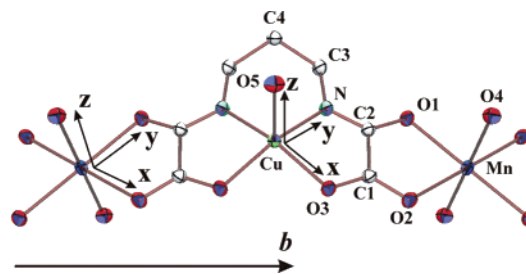|	model	R (%)	R_w (%)	G.O.F.	N_{obs}	N_{par}
$(I > 0)$	I (promolecule)	6.38	7.19	1.70	4567	115
	II (multipolar)	5.51	5.16	1.22	4567	326
$(I > 3\,\sigma(I))$	I (promolecule)	4.11	6.66	1.85	3297	115
	II (multipolar)	3.24	4.44	1.24	3297	326

high-resolution shells, showing the consistency of the whole data set. Intensity uncertainties were individually re-estimated based on the normal distribution of the multiple measured reflections, taking advantage of the large data redundancy. More details about the experimental settings and crystal data are reported in Table 1.

Electron Density Modeling. An accurate structural model was derived by spherical atom refinement of position and anisotropic thermal parameters of non-hydrogen atoms against high order data $(\sin(\theta)/\lambda > 0.8$ Å⁻¹, $N_{obs} = 1519$, $N_{par} = 115$, $R(F) = 12.72\%)$. This high order procedure prevents biasing the atomic displacement parameters (ADPs) by the deformation of the valence ED. Hydrogen atom positions and isotropic ADPs were obtained from an all data refinement; then O–H and C–H distances were adjusted to the usual neutron values (C–H = 1.08 Å and O–H = 0.99 Å)[37] leading to the "Independent Atom Model" or promolecule (model 1, Table 2), sum of isolated neutral spherical atom EDs.

To take into account the deformation of the atomic valence electron shell, the ED was further refined according to the multipole model.[38] We used the Hansen–Coppens formalism, as implemented in MOLLY,[39] in which the total ED is decomposed into pseudo-atomic contributions as

$$\rho(\vec{r}) = \rho_{core}(r) + P_v\kappa^3\rho_{val}(\kappa r) + \sum_{l=0}^{l_{max}}\kappa'^3 R_l(\kappa' r)\sum_{m=0}^{+l} P_{lm\pm}y_{lm\pm}(\theta,\varphi)$$

where $\rho_{core}(r)$ and $\rho_{val}(r)$ are spherically averaged core and valence EDs calculated from Clementi Hartree–Fock wave functions for ground-state isolated atoms.[40] κ and κ' are contraction–expansion parameters, and P_v is the atomic valence shell population. The deformation of the

(37) Allen, F. H. *Acta Cryst.* **1986**, *B42*, 515.
(38) Stewart, R. F. *J. Chem. Phys.* **1973**, *58*, 1668.
(39) Hansen, N. K.; Coppens, P. *Acta Cryst.* **1978**, *A34*, 909.
(40) Clementi, E.; Roetti, C. *At. Data Nucl. Data Tables* **1974**, *14*, 177.

Figure 1. Ortep[67] view and labeling of the chain structure. Thermal displacement ellipsoids are plotted at the 50% probability level. O4 and O5 are the oxygen atoms of the coordinated water molecules. Hydrogen atoms and noncoordinated water molecules are omitted for clarity. Mn and Cu local coordinate systems are also given.

valence ED is projected on the basis of real spherical harmonics ($y_{lm\pm}$) using Slater type radial functions

$$\left(R_l(r) = \frac{\xi_l^{n_1+3}}{(n_1 + 2)!}r^{n_1}e^{-\xi_l r}\right)$$

To a good approximation, the atomic inner shells are not affected by chemical bonding (frozen core approximation). Initial radial functions coefficients ξ_l were taken from the energy optimized Slater-type exponents:[41] $(n_1 = 4, 4, 4, 4; \xi_l = 7.0$ bohr⁻¹) for Cu and Mn, $(n_1 = 2, 2, 3; \xi_l = 2.5$ bohr⁻¹) for N, $(n_1 = 2, 2, 3; \xi_l = 3.3$ bohr⁻¹) for O, $(n_1 = 2, 2, 3; \xi_l = 3.14$ bohr⁻¹) for C, and $(n_1 = 2; \xi_l = 2.28$ bohr⁻¹) for H. The multipolar expansion was limited to $l_{max} = 3$ (octupole) for N, C, and O; $l_{max} = 1$ (dipole) for H; and $l_{max} = 4$ (hexadecapole) for Cu and Mn. Anomalous dispersion coefficients were taken from the International Tables for Crystallography.[42]

Starting from the promolecule model (model I), we fitted valence populations and κ parameters sequentially using all data $(I > 0)$. An electroneutrality constraint was applied to the unit cell; as charge transfer and electron delocalization effects might be expected from Mn and Cu to the coordinated and noncoordinated water molecules, no neutrality constraints were applied on the water molecules. For Cu and Mn, preliminary tests were performed, using two independent monopoles P_v and P_{00} for the 4s and 3d electrons, respectively. The Cu and Mn 4s scattering factors decrease very rapidly versus resolution, leading to difficulties in the refinement of the corresponding P_v and P_{00} parameters. Despite expected instabilities observed during $(P_v$ and $P_{00})$ refinement, the Cu(4s) population decreased to almost 0, whereas the Mn(4s) population remained close to 2. Therefore, the corresponding Cu and Mn valence radial scattering factors were calculated using 4s⁰3d⁹ and 4s²3d⁵ electron configurations respectively and one monopole only (P_v) was finally refined for each metal; furthermore, only monopole, quadrupole and hexadecapole functions were allowed to vary assuming no 3d4p and 4s4p hybridization. Except the crystallographic mirror plane for Cu (see below), no other chemical symmetry constraint was applied on the Mn and Cu multipoles. The local coordinate systems (Figure 1) were defined according to the coordination spheres: pyramidal for Cu (z axis along the apical direction) and octahedral for Mn (z axis along the Mn–O4 direction). In the first steps, chemically equivalent hydrogen atoms were modeled using a single set of multipole parameters (P_v, P_{10}, where P_{10} is the dipole population along the H–X bond (X = C,O)). Related to the isotropic thermal motion model used for hydrogen atoms, this dipole is the only significant contribution to the deformation density of H (as checked). The chemical equivalence constraint was relaxed at the end of refinement in order to better model hydrogen atoms involved in intermolecular interactions.

Agreement factors are summarized in Table 2. With the introduction of the aspherical multipolar model, the agreement indices decrease from

(41) Clementi, E.; Raimondi, D. L. *J. Chem. Phys.* **1963**, *38*, 2686.
(42) *International Tables for Crystallography*; Reidel: Dordrecht 1992; Vol. C, p 219.
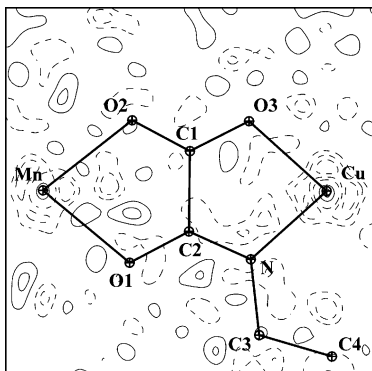
Figure 2. Residual electron density in the oxamato bridge plane at the end of multipolar refinement. Contour levels: 0.1 eÅ^{-3}, positive solid lines and negative dashed ($I > 3\sigma(I)$, $S < 0.8$ Å^{-1}).

6.38% to 5.51% for R and from 7.19% to 5.16% for R_w (all data). Even with the full multipolar model, the agreement factors are nevertheless rather high, due to the limited crystal quality of the samples. Figure 2 shows the residual electron density (difference between observed and modeled electron densities) at the end of multipolar refinement, given by

$$\Delta\rho_{resid}(\vec{r}) = \frac{1}{V}\sum_{h,k,l}\left(\frac{1}{k}\left|F_{obs}(hkl)\right| - \left|F_{calc}^{mult}(hkl)\right|\right)e^{i\varphi_{mult}}e^{-2i\pi(\vec{H}.\vec{r})}$$

where V is the unit cell volume, F_{obs} and F_{calc} are structure factors observed and calculated using the multipolar model, respectively, φ_{mult} is the structure factor phase calculated using the multipolar model, and the sum runs over all reflections ($I > 0$).

The residual density at the end of multipolar refinement is however flat in the interchain regions and on the oxamato bridge; residual density does not exceed 0.2 eÅ^{-3} ($2*\sigma(\rho)$) at nearly 0.7 Å from O1. The regions close to Mn and Cu nuclei exhibit some residual density not taken into account by the multipolar model, which represents a limitation of our model (or data) in the present case. The estimated average errors in the experimental density are

$$\sigma_1(\rho) = \left(\frac{1}{V}\sum_{h,k,l}(\sigma(F_{obs}(hkl)))^2\right)^{1/2} = 0.10e\text{Å}^{-3}$$

and

$$\sigma_2(\rho) = \left(\frac{1}{V}\sum_{h,k,l}(|F_{obs}(hkl)| - |F_{calc}^{mult}(hkl)|)^2\right)^{1/2} = 0.11e\text{Å}^{-3}$$

where V is the unit cell volume, F_{obs} and F_{calc} are structure factors observed and calculated using the multipolar model, respectively, and the sum runs over all reflections ($I > 0$).

Topological Analysis of the Electron Density. A complete and quantitative study of the ED can be performed through the topological analysis following the "Atoms in Molecules" theory.[43–45] Interatomic interactions are characterized by the properties of the ED and its laplacian at bond critical points, noted as BCPs, where the gradient of the ED vanishes. Two bonded atoms are moreover connected by a line of maximum ED, called a bond path. The ellipticity of the bond, defined as $\epsilon = 1 - |\lambda_1/\lambda_2|$, where λ_1 and λ_2 are the principal curvatures of the ED in the plane perpendicular to the bond ($\lambda_1 < \lambda_2$), is a measure of the departure from cylindrical symmetry of the ED at the BCP. The laplacian of the ED indicates regions of electron accumulations

($\nabla^2\rho < 0$) and depletions ($\nabla^2\rho > 0$); peaks of negative laplacian, called valence shell charge concentrations (VSCCs), depict the deformation of the atomic valence shell due to bonding and hybridization. The atomic ED is enclosed by interatomic surfaces, defined by the zero flux condition of the gradient field, delimiting atomic basins. The integration of the ED over the atomic basins yields topological atomic charges.

As discussed by Bader and co-workers,[43–45] the topological analysis of the ED allows deriving local energetic properties. Abramov[46] proposed an evaluation of the kinetic energy density $G(\vec{r}_{CP})$ at a given BCP as a function of $\rho(\vec{r}_{CP})$ and $\nabla^2\rho(\vec{r}_{CP})$:

$$G(\vec{r}_{CP}) = (3/10)(3\pi^2)^{2/3}(\rho(\vec{r}_{CP}))^{5/3} + (1/6)\nabla^2\rho(\vec{r}_{CP})$$

This local relationship is valid for closed-shell interactions in medium-range distances from the atoms (0.5 to 2 Å). It is accurate for hydrogen bonds ($\rho(\vec{r}_{CP}) \approx 0.2$eÅ^{-3})[47,48] and should be applied with caution to coordination interactions. The potential energy density $V(\vec{r}_{CP})$ at the BCP is related to $G(\vec{r})$ through the local virial theorem.[43] All topological properties of the ED, as well as the integration over the atomic basins, have been performed using program NEWPROP[49,50] and are given in Tables 3 and 4.

Results

Crystal Structure. The crystal structure of MnCu(pba)-(H$_2$O)$_3$·2H$_2$O has already been published by Pei et al.[16] and by Baron et al.;[17] we just recall here the main features observed at 114 K, needed for a clear understanding of the ED analysis. The structure is built up from infinite bimetallic Mn–Cu chains, running along the b axis in which Mn and Cu are connected by a bis-bidentate oxamato ligand (Figure 1). Mn lies on an inversion center in an elongated octahedral coordination. Water molecules (O4H$_2$) are located in the elongated apical directions (⟨Mn–O apical⟩ = 2.201(1) Å), whereas the axial positions are occupied by the O1 and O2 atoms of the oxamato bridge (⟨Mn–O basal⟩ = 2.166(1) Å). Cu is located on a crystallographic mirror plane in a CuN$_2$O$_3$ pyramidal surrounding, coordinated by one water molecule (O5H$_2$) in the apical direction and two O3 and N atoms of two symmetry related oxamato groups in the basal plane. Cu lies 0.2475(5) Å out of the basal plane in the direction of the water molecule.

The parallel chains are connected in the a and c directions by four short hydrogen bonds involving the O1 and O2 atoms of the oxamato bridge and the coordinated and non coordinated water molecules. The O···H distances range from 1.71(1) Å to 2.04(1) Å with corresponding O–H···O angles from 153.9(1)° to 170.6(1)°. Bonding distances are summarized in Table 3, together with the BCP's properties. The quasi one-dimensional crystal structure involves similar distances between the magnetic centers within and between the chains, $d_{Mn···Cu} = 5.4220(2)$ Å and $d_{Mn···Mn}$ ($d_{Cu···Cu}$) = 5.1861(2) Å respectively.

Electron Density Distribution along the Chains. In the following part, we discuss the ED distribution, dividing the chain into three characteristic regions.

1. Bridging Region. The static electron deformation density, as defined by the difference between multipole (model II) and

(43) Bader, R. F. W. *Atoms in molecules: a quantum theory*. The International Series Monographs in Chemistry. Oxford: Clarendon Press: 1990.
(44) Bader, R. F. W.; Essen, H. *J. Chem. Phys.* **1984**, *80* (5), 1943.
(45) Bader, R. F. W.; Preston, H. J. T. *Int. J. Quantum Chem.* **1969**, *3*, 327.
(46) Abramov, Y. A. *Acta Crystallogr.* **1997**, *A53*, 264.
(47) Espinosa, E.; Molins, E.; Lecomte, C. *Chem. Phys. Lett.* **1998**, *285*, 170.
(48) Espinosa, E.; Lecomte, C.; Molins, E. *Chem. Phys. Lett.* **1999**, *300*, 745.
(49) Souhassou, M.; Blessing, R. H. *J. Appl. Cryst.* **1999**, *32*, 210.
(50) Katan, C.; Rabiller, P.; Lecomte, C.; Guezo, M.; Oison, V.; Souhassou, M. *J. Appl. Cryst.* **2003**, *36*, 65.

Table 3. Topological Properties of the Electron Density at the Bond and Ring Critical Points[a]

bond (X–Y)	d(X–Y) (Å)	d(X–CP) (Å)	d(Y–CP) (Å)	$\rho(\vec{r}_{cp})$ (eÅ⁻³)	$\nabla^2\rho(\vec{r}_{cp})$ (eÅ⁻⁵)	ϵ	$G(\vec{r}_{cp})$ (kJ mol⁻¹)	$V(\vec{r}_{cp})$ (kJ mol⁻¹)	$\rho(\vec{r}_{cp}) - \rho_{prom}(\vec{r}_{cp})$ (eÅ⁻³)
Cu–O3	1.996(1)	0.92	1.08	0.62	8.7		298.40	−360.71	0.17
Cu–N	1.948(1)	0.91	1.04	0.74	8.0		334.96	−451.53	0.22
Cu–O5	2.271(1)	1.10	1.17	0.32	4.3		125.25	−132.87	0.10
Mn–O1	2.160(1)	1.08	1.08	0.34	6.2		165.08	−160.25	0.07
Mn–O2	2.172(1)	1.05	1.12	0.40	5.9		175.39	−189.58	0.12
Mn–O4	2.201(1)	1.06	1.14	0.37	5.5		159.13	−169.03	0.12
C1–C2	1.535(2)	0.77	0.77	1.80	−16.9	0.31			0.68
C2–O1	1.282(2)	0.51	0.78	2.40	−26.1	0.29			0.48
C2–N	1.298(2)	0.59	0.71	2.36	−19.4	0.30			0.52
C1–O3	1.252(2)	0.47	0.80	2.43	−22.2	0.26			0.45
C1–O2	1.267(2)	0.57	0.68	2.48	−8.3	0.27			0.45
N–C3	1.465(2)	0.79	0.68	1.59	−5.1	0.09			0.21
C3–C4	1.523(2)	0.91	0.62	1.49	−9.5	0.08			0.34
ring1 CuNC2C1O3				0.24	3.1				0.04
ring2 MnO1C2C1O2				0.14	2.6				0.02

bond (X–Y)	d(X–Y) (Å)	d(O···O)* (Å)	O–H···O* (deg)	direction of connection*	d(X–CP) (Å)	d(Y–CP) (Å)	$\rho(\vec{r}_{cp})$ (eÅ⁻³)	$\nabla^2\rho(\vec{r}_{cp})$ (eÅ⁻⁵)	$G(\vec{r}_{cp})$ (kJ mol⁻¹)	$V(\vec{r}_{cp})$ (kJ mol⁻¹)	$\rho(\vec{r}_{cp}) - \rho_{prom}(\vec{r}_{cp})$ (eÅ⁻³)
O4–H2···O1	1.85(1)	2.816(1)	163.1(1)	c	0.68	1.18	0.17	3.8	85	−67	−0.09
O6–H8···O2	1.87(1)	2.793(1)	154.3(1)	c	0.66	1.22	0.15	4.2	90	−65	−0.10
O4–H6···O6	1.71(1)	2.717(2)	170.6(1)	c	0.63	1.10	0.30	3.9	114	−120	−0.06
O6–H5···O1	2.04(1)	2.967(2)	153.9(1)	a	0.78	1.26	0.19	1.8	52	−56	+0.02

[a] λ_i are the principal curvatures of the ED at BCP. $\epsilon = 1 - |\lambda_1/\lambda_2|$ is the ellipticity of the bond at the BCP. The ellipticity at the BCPs is only given for C–O, C–N, and C–C bonds. $G(\vec{r}_{cp})$ and $V(\vec{r}_{cp})$ are the kinetic and potential energy densities at the BCP (see text). ρ_{prom} is the ED of the promolecule (model I). * applies to hydrogen bonds only.

Table 4. Atomic and Fragment Topological Charges (e) and Volumes (Å³)[a]

	Cu	Mn	O1	O2	O3	N	C1
charge	+1.56	+1.45	−0.97	−0.87	−0.80	−1.15	+1.38
volume	9.46	10.80	13.72	16.44	14.39	13.89	4.90

	C2	C3	C3H₂	C4	C4H₂	oxamato group
charge	+0.87	−0.20	+0.30	−0.78	−0.16	−1.54
volume	7.34	11.35	23.24	11.74	19.70	70.68

	O4	H₂O4	O5	H₂O5	O6	H₂O6
charge	−1.65	−0.34	−1.32	0.06	−1.35	0.04
volume	22.28	25.58	20.02	23.70	21.86	25.32

[a] The total charge and integrated volume summed over the unit cell are −0.072 e and 176.659 Å³, respectively, which represent total errors of 0.07 and 0.07 %, respectively, due to the integration procedure.

promolecule (model I) EDs, is shown in Figure 3a in the plane of the oxamato group.

$$\Delta\rho_{stat}(\vec{r}) = \rho_{mult}(\vec{r}) - \rho_{prom}(\vec{r}) = P_v\kappa^3\rho_{val}(\kappa r) - N_v\rho_{val}(r) + \sum_{l=0}^{l_{max}}\kappa'^3 R_l(\kappa'r)\sum_{m=0}^{l}P_{lm\pm}y_{lm\pm}(\theta,\varphi)$$

The C–C, C–N, and C–O bonds exhibit usual characteristics with maximum deformation density in the bonds. With C1–C2 being nonpolar, the density maximum is well centered in the bond, in contrast to the C–O and C–N bonds for which the maximum density is systematically shifted toward the carbon atom. Similar polarization effects were observed in other molecules containing N–O groups.[28,30,51,52]

These observations are supported by the topological analysis (Table 3): the C1–C2 BCP lies in the middle of the bond (0.77

Å), whereas, in all C–O and C–N bonds, the BCP is shifted toward C. For all oxamato bonds, the ED, ellipticity, and laplacian at BCP are higher than those for corresponding single bonds; the ED, ellipticity, and laplacian at C1–C2 BCP are larger than those for the C3–C4 single bond, even though the bond distance is longer (1.535(2) Å for C1–C2 and 1.523(2) Å for C3–C4). The C1–C2 topological characteristics are close to those observed for conjugated C–C bonds such as in the nitronyl ring of Nit(SMe)Ph ($\rho_{CP} = 1.80$ eÅ⁻³ and $\nabla^2\rho_{CP} = -13.2$ eÅ⁻⁵)[28] but are nevertheless lower than those for aromatic bonds[28,53] ($\rho_{CP} \approx 2.1$ eÅ⁻³ and $\nabla^2\rho_{CP} \approx -18$ eÅ⁻⁵). The ED and laplacian at C2–N BCP are larger than those for the C3–N bond; they compare to those observed in Nit(SMe)Ph and are correlated to the bond length evolution: 1.298(2) Å for C2–N, 1.465(2) Å for C3–N, and 1.3555(5) Å for Nit(SMe)Ph. The ED and laplacian at the C–O BCPs are high but lower than those observed for noncoordinated C–O bonds.[54] The high ellipticities of the C–O, C2–N, and C1–C2 bonds (from 0.26 to 0.31) indicate large ED π asymmetry. By comparison with the promolecule (model I), the ED at all C–O, C–C, and C–N BCPs increases, due to the formation of covalent bonds; C1–C2 exhibits the largest buildup of ED ($\Delta\rho = +0.68$ eÅ⁻³), whereas the single N–C3 and C3–C4 bonds present the smallest increase. The change is the same for all three C–O bonds (∼0.46 eÅ⁻³), even though they are not coordinated to the same metal: O1–Mn, O2–Mn, and O3–Cu. All these topological features of the oxamato moiety characterize large conjugation effects over the whole bis-bidentate ligand.

The laplacian of the ED is given in Figure 4. For all atoms of the oxamato group, peaks of negative laplacian (VSCCs) are located at nearly 0.5 Å from the nuclei, in the interatomic

(51) Kubicki, M.; Borowiak, T.; Dutkiewicz, G.; Souhassou, M.; Jelsch, C.; Lecomte, C. *J. Phys. Chem.* **2002**, *106(14)*, 3706.
(52) Zhurova, E.; Pinkerton, A. *Acta Crystallogr.* **2001**, *B57*, 359.

(53) Volkov, A.; Abramov, Y.; Coppens, P.; Gatti, C. *Acta Crystallogr.* **2000**, *A56*, 332.
(54) Benabicha, F.; Pichon-Pesme, V.; Jelsch, C.; Lecomte, C.; Khmou, A. *Acta Crystallogr.* **2000**, *B56*, 155.
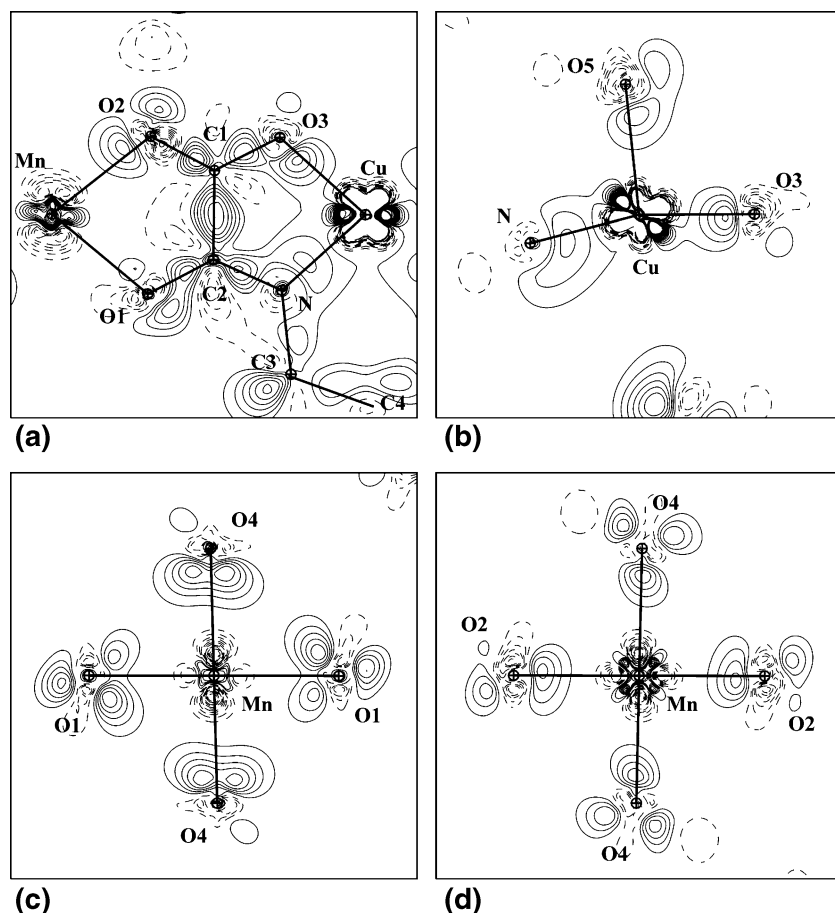
Figure 3. Static deformation density in the oxamato bridge plane (a), Cu−O3−O5 plane (b), Mn−O2−O4 plane (c), and Mn−O1−O4 plane (d). Contour levels as in Figure 2.

directions. C1 and C2 exhibit three VSCCs located in the oxamato plane pointing toward their bonded neighbor atoms, characteristic of sp^2 hybridization. The oxamato nitrogen and oxygen atoms exhibit VSCCs almost perpendicular to the C−N and C−O bonds, corresponding to the two N and O lone pairs.

According to the topological atomic charges (Table 4), the oxamato bridge carries a −1.54 charge and exhibits a large electron polarization. The C atoms are positive, whereas negative charges are accumulated on the O and N atoms, resulting from two adding effects: larger electronegativity of N and O than that of C and Mn−O, Cu−N, and Cu−O coordination interactions, as discussed above.

The comparison of the oxamato ED with that of the oxalato group in $NaHC_2O_4 \cdot H_2O$[55] and of oxalic acid[56] shows the strong influence of the metal coordination. The static deformation density of the central C−C bond in oxalic acid (0.65 e$Å^{-3}$) is similar to the oxamato C1−C2 bond, with a longer bond length (1.5432(4) Å versus 1.535(2) Å). On the other hand, the static deformation density in the C−O oxamato bonds is lower than those for C−O and C−OH bonds in $NaHC_2O_4 \cdot H_2O$ and oxalic acid (0.60−0.80 e$Å^{-3}$). The coordination interactions thus induce a redistribution of ED from the C−O oxamato bonds to the O−Cu and O−Mn regions.

2. Cu Region. The static deformation density in the CuO_5O_3N plane is given in Figure 3b: a large ED depletion in the copper electron valence shell, due to electronic repulsion by crystal field effects, shows up in the Cu−O and Cu−N interaction directions. The deformation is similar in the N and O3 directions, while a smaller effect is revealed in the apical direction (Cu−O5), in line with a longer coordination distance (2.271(1) Å versus 1.996(1) Å and 1.948(1) Å). Correlatively, positive deformation peaks are located in the diagonal directions. These deformation density features are the signature of $d_{x^2-y^2}$ orbital depletion and, to a lower extent, of that of the d_{z^2} orbital, which are destabilized compared to the d_{xz} (d_{yz}) and d_{xy} orbitals in agreement with a pyramidal surrounding (local coordinate system given in Figure 1). The 3d orbital populations, as derived from the Cu multipolar modeling[57] (Table 5), reflect the pyramidal environment of copper with higher d_{xy}, d_{yz}, and d_{xz} populations than that of d_{z^2}. The $d_{x^2-y^2}$ orbital is the least populated orbital due to electronic repulsion with O3 and N lone pairs in the basal plane. For a $3d^9$ electron configuration and from crystal field considerations only, one might explain these d orbital populations, keeping in mind that our estimation takes also into account the σ and π donation from and toward Cu according to the Dewar−Chatt−Duncanson metal−ligand model.[58,59] Many experimental ED studies agree with this model

(55) Delaplane, R. G.; Tellgren, R.; Olovsson, I. *Acta Crystallogr.* **1990**, *B46*, 361.
(56) Coppens, P.; Dam, J.; Harkema, S.; Feil, D.; Feld, R.; Lehmann, M. S.; Goddard, R.; Krüger, C.; Hellner, E.; Johansen, H.; Larsen, F. K.; Koetzle, T. F.; McMullan, R. K.; Maslen, E. N.; Stevens, E. D. *Acta Crystallogr.* **1984**, *A40*, 184.

(57) Holladay, A.; Leung, P.; Coppens, P. *Acta Crystallogr.* **1983**, *A39*, 377.
(58) Dewar, M. J. S. *Bull. Soc. Chim. Fr.* **1951**, C71.
(59) Chatt, J.; Duncanson, L. A. *J. Chem. Soc.* **1953**, 2939.
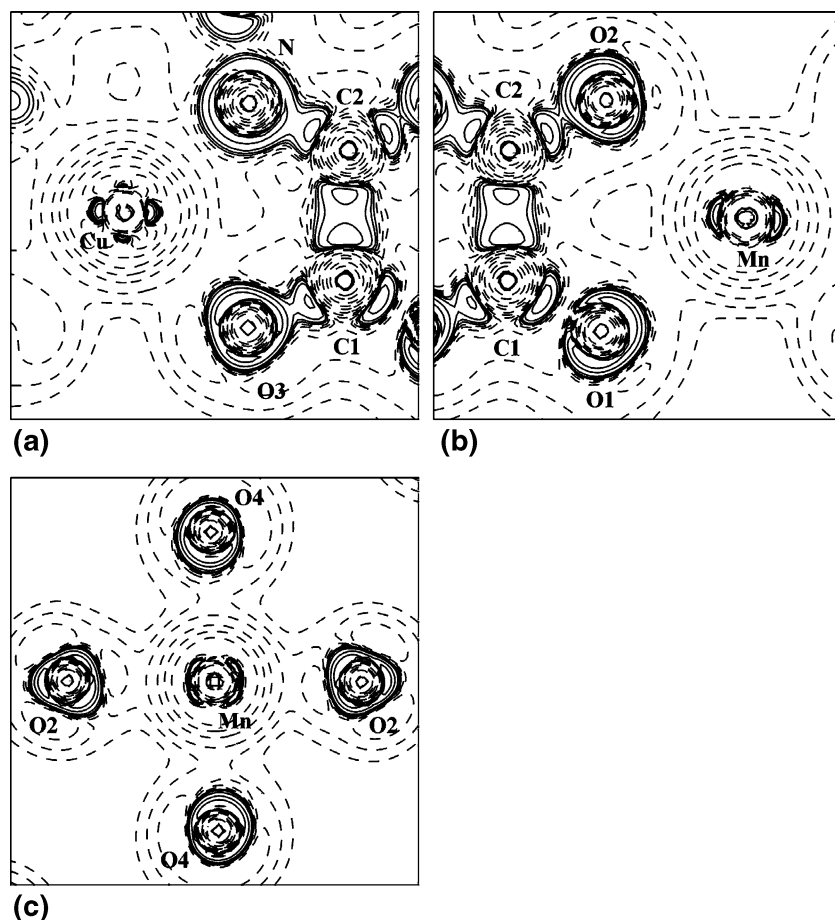
Figure 4. Contour map of $-\nabla^2\rho$ in the Cu−O3−N plane (a), Mn−O2−O1 plane, (b) and Mn−O2−O4 plane (c). Contour levels at 2×10^n, 4×10^n, and 8×10^n eÅ^{-5} ($n = -3, -2, -1, 0, 1$), positive solid lines and negative dashed.

Table 5. 3d Atomic Orbital Populations (in %) for Cu and Mn[a]

	$d_{x^2-y^2}$ (%)	d_{z^2} (%)	d_{xy}(%)	d_{xz}(%)	d_{yz}(%)
Cu	11.1(3)	16.5(3)	23.2(3)	24.6(3)	24.6(3)
Mn	17.8(3)	16.4(3)	20.8(3)	22.5(3)	22.5(3)

[a] The corresponding local coordinate systems are given in Figure 1.

like, for example, iron and cobalt porphyrins[60,61] and coordination complexes.[62] The same conclusions are drawn by inspection of the VSCCs around the Cu atom (Figure 4); they are located in the d_{xy}, d_{yz}, and d_{xz} directions with a maximum at 0.3 Å from Cu. The coordinating N and O3 atoms exhibit positive deformation density toward Cu, corresponding to their lone pairs. The charge densities in the Cu−N and Cu−O3 directions are however different. The nitrogen positive deformation density is spread along and around the N−Cu axis, with a maximum of 0.3 eÅ^{-3}, whereas the O3 deformation density is more compact and well localized closer to O3 with a higher maximum (0.5 eÅ^{-3}). The overlap between the Cu and N atomic orbitals is therefore expected to be higher than that occurring between O3 and Cu; this is confirmed by the topological analysis of the ED (see below). The topological charge obtained for the apical water molecule O5H$_2$ is very low (+0.04), indicating no Cu d$_{z^2}$ orbital σ donation.

All coordination interactions involving Cu are characterized by the existence of a bond path on which lies a BCP with positive laplacian, indicating mainly closed-shell interactions, as usually observed for metal−ligand interactions. The BCPs in the basal Cu−N and Cu−O3 directions are located at nearly the same distance from Cu (0.92 Å); the ED at BCP is higher for the Cu−N bonds, corresponding to a higher covalent contribution. This ED is also higher than that observed in a *trans*-bis(cyanamidonitrato-N:O)bis-(imidazole-N^3)copper(II) complex[63] which exhibits longer Cu−N bonds ($d = 1.9660(4)$ Å, $\rho_{CP} = 0.62$ eÅ^{-3} and $d = 2.0273(5)$ Å, $\rho_{CP} = 0.49$ eÅ^{-3}). The smaller ED at BCP in the apical direction (0.32 e Å^{-3}) agrees with the longer and therefore weaker Cu−O5 interactions. The degree of covalency thus increases from Cu−O5 to Cu−O3 and Cu−N coordination interactions. In agreement with the deformation density, the nitrogen VSCC directed toward Cu is diffuse (Figure 4a), whereas O3 and O5 VSCCs are well localized along the coordination directions (Figure 3b and Supporting Information).

The kinetic $G(\vec{r})$ and potential $V(\vec{r})$ energy densities are high at Cu−N and Cu−O3 BCPs (Table 3), in agreement with significant ED buildup by the reference to the promolecule (model I): $\rho_{mult} - \rho_{prom} = +0.22$ and $+0.17$ eÅ^{-3}, respectively. Moreover, the potential energy density overcomes the kinetic energy density by at least 60 kJ mol^{-1}. As less ED is

(60) Lecomte, C.; Blessing, R. H.; Coppens, P.; Tabard, A. *J. Am. Chem. Soc.* **1986**, *108*, 6942.
(61) Lecomte, C.; Rohmer, M. M.; Benard, M. In *The Porphyrin Handbook*, 7; Kadish, K. M., Smith, K. M., Guilard, R., Eds; Academic Press: 1999.
(62) Macchi, P.; Proserpio, D. M.; Sironi, A. *J. Am. Chem. Soc.* **1998**, *120*, 1447.
(63) Kozisek, J.; Hansen, N. K.; Fuess, H. *Acta Crystallogr.* **2002**, *B58*, 463.

concentrated along the bond path, the energy densities are lower for the Cu—O5 bond (the total energy is only −7 kJ mol^{-1}).

3. Mn Region. Compared to Cu, Mn exhibits a smaller but significant negative deformation density along the Mn—O bonds and positive lobes in the diagonal directions (Figure 3a). A similar deformation density of the Mn valence shell has been reported by Bianchi et al. for Mn$_2$(CO)$_{10}$.[64] O1, O2, and O4 oxygen atoms present lone pairs positive deformation density in the Mn direction (Figure 3, maximum 0.4−0.5 e Å^{-3}). These accumulations are elongated in the plane perpendicular to the O—Mn axis; this is the main characteristic. Compared to O1 and O4, the nonsplitting of the O2 density may be a consequence of the limited resolution of the experiment. The topological properties of all Mn—O bonds are similar, characteristic of the almost regular Mn octahedral environment; as a consequence, the Mn t$_{2g}$ orbitals are more populated than the e$_g$ ones due to crystal field repulsion. The BCPs are located slightly closer to Mn than O ($\langle d_{Mn-CP}\rangle$ = 1.06(2) Å), and the average density at BCP (0.37(3) e Å^{-3}) is lower than those for the Cu—O3 and Cu—N bonds (0.62 and 0.74 e Å^{-3}), enlightening more ionic interactions. The increase of ED at the Mn—O BCPs compared to the promolecule is also smaller than that for the copper coordination bonds. VSCCs are located around Mn, corresponding to an accumulation of ED in diagonal directions. The Mn 3d orbitals are less contracted than those for Cu; the maxima of negative laplacian (VSCCs) are located at a larger distance from the nucleus, nearly 0.4 Å (0.3 Å for Cu). O1 and O4 exhibit one VSCC directed toward Mn, corresponding to the coordination interactions, while O2 presents two less resolved VSCCs. The O4 VSCC is also elongated in the Mn—O4—O2 plane. The kinetic and potential energy densities are half the corresponding energy densities for copper bonds; they are in the same range for the three Mn—O BCPs, showing isotropicity of the Mn—O coordination bonds. In conclusion, all topological features demonstrate the lower covalency and therefore lower directionality of Mn—O interactions compared to those involving the copper atom.

Interchain Hydrogen Bonds. Pei et al.[16] have shown from the magnetic behavior of MnCu(pba)(H$_2$O)$_3$·2H$_2$O a departure from one-dimensional antiferromagnetic exchange coupling at very low temperature (below 2.3 K). Indeed, weak interchain interactions superimpose to the intrachain coupling, which could be related to hydrogen bonds. We have shown in our previous studies on organic radicals [28,29] that careful investigation of the electron density topology in intermolecular (or interchain) regions helps in locating and analyzing weak interaction pathways. In MnCu(pba)(H$_2$O)$_3$·2H$_2$O, the crystal structure suggests the presence of four interchain hydrogen bonds whose structural properties are summarized in Table 3. As shown in Figure 5, bridges of ED connect the chains in the hydrogen bond regions. The gradient field of the ED (Figure 6 and Supporting Information) exhibits typical topological features of hydrogen bonding in all O···H directions: an interatomic surface and a bond path linking O and H on which lies a BCP. The ED values at BCPs range from 0.15 eÅ^{-3} to 0.30 eÅ^{-3} and indicate medium strong hydrogen bonds, whereas the positive sign of the corresponding laplacians (from 1.8 eÅ^{-5} to 4.2 eÅ^{-5}) is characteristic of closed shell interactions, as usual for this type of hydrogen bonds. The EDs at BCPs are slightly lower than

(64) Bianchi, R.; Gervasio, G.; Marabello, D. *Inorg. Chem.* **2000**, *39*, 2360.
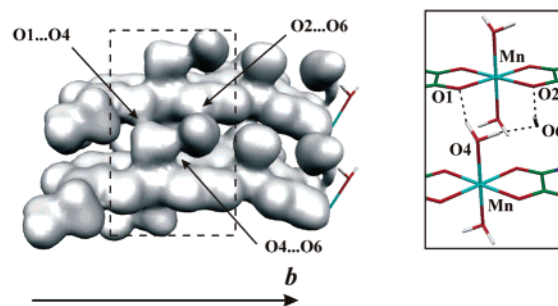
Figure 5. Total electron density in the interchain region (isocontour 0.1 eÅ^{-3}). The interchain hydrogen bonds (O1···O4, O2···O6, and O4···O6) are shown in the insert.
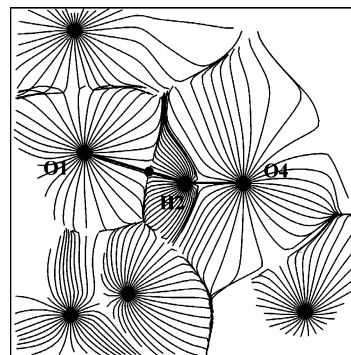
Figure 6. Gradient trajectories of the electron density in the O1···H2—O4 hydrogen bond region.

those obtained in the promolecule model, as previously observed in other hydrogen bond studies.[29] The kinetic $G(\vec{r})$ and potential $V(\vec{r})$ energy densities at BCPs (Table 3) range from +52 to +114 kJ mol^{-1} and from −56 to −120 kJ mol^{-1}, respectively, in quite good agreement with the exponential fit of the energy density versus the O···H distance derived by Espinosa et al.[47] According to these energy densities, the O4—H6···O6 hydrogen bond is the strongest, as predicted from the shortest bond length.

Discussion

Mn—Cu Interactions. A first question arises about the mode of Mn—Cu interactions along the chains: it could be either global or well localized along bond paths. In the first case, a single critical point (CP) would be observed between the oxamato bridge and the metal atoms. This situation would be similar to T-shape interactions between a metal and a C—C bond, for which a bond path would link the metal to the center of the C—C bond, as discussed by Macchi et al.[62] The second situation would consist of a bond path and a BCP in the Cu—O3 and Cu—N directions as well as in the Mn—O1 and Mn—O2 directions. Correlatively, a ring critical point (RCP, minimum of ED in the ring plane and maximum in the perpendicular direction) should be localized in the Cu—O3—C1—C2—N and Mn—O1—C2—C1—O2 rings. Figure 7 gives a clear answer to this question. All Cu—N, Cu—O3, Mn—O1, and Mn—O2 directions exhibit the same topological features such as sharing an interatomic surface, presence of bond path, and BCP which are definite clues of localized interatomic bonds. In addition, an RCP is located in each five atom ring. We have shown in the previous sections that both metals exhibit positive atomic charges: +1.56 e and +1.45 e for Cu and Mn, respectively, to neutralize the oxamato negative charge. This charge transfer from both metals to the bridge is slightly higher for Cu than
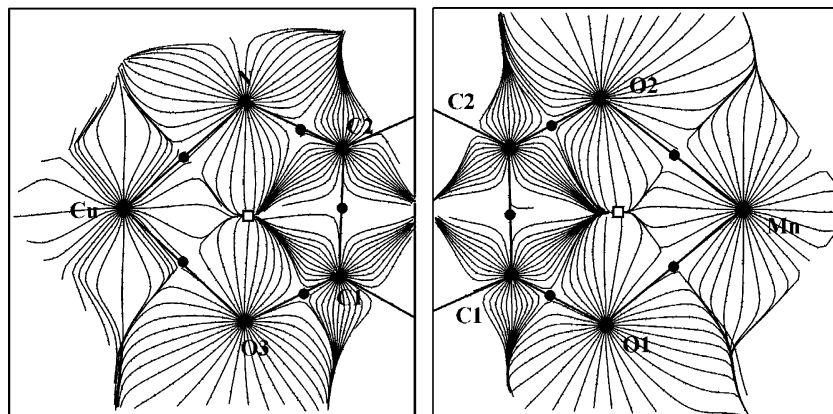
Figure 7. Gradient trajectories of the electron density and position of the critical points along the bimetallic chain. Bond critical points are depicted as full circles and ring critical points as open squares.
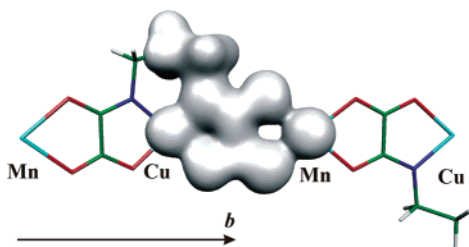
Figure 8. Total electron density along the bimetallic chain (isocontour 0.25 eÅ^{-3}).

for Mn. The bridge undergoes in turn a charge polarization due to the metal–O and metal–N interactions which drag electrons from the inner C atoms to the coordinating N and O atoms. The overall orbital overlap is higher on the copper side of the oxamato bridge than on the manganese side (Figure 8), as also revealed by the ED difference at the corresponding RCPs (0.24 e Å^{-3} and 0.14 e Å^{-3} for Cu and Mn, respectively).

Relations between Electron Density, Spin Density, and Magnetic Properties. The electron and spin density distributions are complementary for the analysis of the chemical bonding since ED describes the behavior of all electrons (core and valence: $\rho(\vec{r}) = \rho_\uparrow(\vec{r}) + \rho_\downarrow(\vec{r})$), whereas spin density describes the unpaired electrons only ($m(\vec{r}) = \rho_\uparrow(\vec{r}) - \rho_\downarrow(\vec{r})$). Thus a combined inspection of both density distributions allows full view of the interatomic and intermolecular interactions.

From polarized neutron diffraction measurements, Baron et al.[17] modeled the spin density distribution using a restricted multipolar model: spherical approximation for Mn and all oxamato bridge atoms, whereas the Cu spin density was refined in a $d_{x^2-y^2}$ orbital. The resulting spin populations are the following: 4.93(3) μ_B, −0.75(2) μ_B, 0.02(1) μ_B, 0.01(1) μ_B, −0.05(1) μ_B, −0.08(1) μ_B, −0.03(2) μ_B, and −0.03(1) μ_B for Mn, Cu, O1, O2, O3, N, C1, and C2, respectively. The calculation of absolute 3d orbital populations, using the method of Holladay et al.,[57] leads to populations slightly greater than 2e for the Cu d_{xy}, d_{yz}, and d_{xz} orbitals. Strictly speaking, this method is valid when no overlap between the metal and the surrounding ligand orbitals is present. The greater than 2 populations found in the present case results therefore from the covalent character of the Cu–N and Cu–O3 bonds as discussed above. Accordingly, if we renormalize the absolute 3d populations for Cu to 2e for the d_{xy}, d_{yz}, and d_{xz} orbitals, this analysis partly supports the polarized neutron result: the copper d_{xy}, d_{yz}, and d_{xz} orbitals are filled with 2.0 e$^-$ (24.6(3)%), whereas the

$d_{x^2-y^2}$ and d_{z^2} are populated with 0.9 (11.1(3)%) and 1.3 e$^-$ (16.5(3)%), respectively. According to Hund's rule, the d_{z^2} orbital is likely to be partly filled by spin up and spin down electrons, whereas $d_{x^2-y^2}$ can accept one single spin electron. In other words, only the $d_{x^2-y^2}$ orbital should present a significant spin population for Cu. To go further in the analysis, a joint neutron and charge density refinement should be performed allowing Cu spin populations on both $d_{x^2-y^2}$ and d_{z^2}. On the other side, assuming an occupation of one electron in the Mn d_{xz} and d_{yz} orbitals results in a total 3d population of 4.4 e$^-$ on Mn, which compares well with the value of 4.93(3) derived from the polarized neutron analysis. Such a difference might be expected from the difficult deconvolution of the 4s and 3d contributions to the Mn valence ED in the X-ray analysis and from the fact that 4.93(3) μ_B represents the combined effects of spin and orbital (which is expected negligible) magnetic moments in the polarized neutron analysis.

The oxamato bridge, as discussed by Baron et al. exhibits spin delocalization, responsible for exchange coupling along the chains, larger on the Cu side than on the Mn side. These features are particularly evident from the present ED study as the charge distribution on the different fragments shows a large charge transfer from both metals to the oxamato bridge. This charge transfer is very large compared to the spin delocalization observed on neutron results, because it involves all electrons. From the topological analysis of the ED along the chains, we have shown that the metal–ligand interactions are stronger on the copper side than on the manganese side, resulting from larger orbital overlap (Figure 8). This is consistent with the larger spin delocalization on O3 and N compared to O1 and O2.

The topological properties of all BCPs of the oxamato bridge show characteristic features of conjugation effects: short bond lengths, high EDs, high laplacians, and high ellipticities. This electron conjugation is necessary to propagate the interactions along the chain; this can be related to a superexchange Mn–Cu coupling mechanism, in addition to the electron (spin) delocalization. Indeed, spin is transferred from Mn and Cu to each oxamato moiety, on which electron conjugation helps exchange coupling between up and down spin electrons. This electron conjugation is of major importance to induce strong intrachain magnetic couplings.[22–24]

Several authors used the concept of overlap between molecular magnetic orbitals to interpret and foresee the interactions

between bridged metal ions. Verdaguer et al.[65] discussed for example the possibility of increasing the exchange interaction through multiatomic bridges, like oxamato, oxalato, and oxamido, and reported that "the less electronegative the atoms of the bridge are, the larger the delocalization of spin density on the bridge is". The ED analysis of $MnCu(pba)(H_2O)_3 \cdot 2H_2O$ presents experimental features which agree with these arguments. According to the experimental spin density, larger spin delocalization is observed on the copper side of the oxamato group, which is related to the strongest Cu-bridge interactions, characterized by a more covalent character than that of Mn-bridge interactions. Moreover, Cu−N bond exhibits more covalent character than Cu−O3; more spin delocalization is therefore expected through the N atom of the oxamato bridge. This conclusion is also in perfect agreement with the theoretical spin density study on the Cu(pba) precursor by Kahn et al.[18] who showed significant orbital overlap between the oxamato bridge and the $Cu(d_{x^2-y^2})$ atomic orbital.

The magnetic measurements of $MnCu(pba)(H_2O)_3 \cdot 2H_2O$ show interchain couplings at very low temperature. Several studies have shown the implication of hydrogen bonds in weak intermolecular exchange interactions, according to the Mc Connell mechanism[66] even though this mechanism is currently controversial. As described in the previous sections, large charge density observed at interchain hydrogen bond CPs indicates that the chains are connected through the coordinated and non coordinated water molecules. Three of the four hydrogen bonds connect the chains through the $O4H_2$ water molecule coordinated to Mn. Actually, dipolar magnetic interactions could be superimposed to these weak interactions, which do not appear on the ED.

Conclusion

The ED distribution of $MnCu(pba)(H_2O)_3 \cdot 2H_2O$ has been derived by high resolution X-ray diffraction using a pseudo-atomic multipolar model. The chemical bondings along the bimetallic chains and between the chains have been analyzed using the "Atoms in Molecules" formalism. This ED study completes the previously reported spin density study of Baron et al. and has been interpreted in terms of magnetic couplings. In the previous works, the spin densities derived from polarized neutron experiments have been interpreted and compared to theoretical calculations. This study allows visualizing experimental electron density properties and enforces the confidence in the theoretical interpretation.

The intrachain interactions are characterized by high charge transfer from Mn and Cu to the oxamato bridge. The oxamato group presents high electron conjugation effects, allowing indirect Mn−Cu magnetic coupling by superexchange. The N, O1, O2, and O3 atomic charges show a strong electron polarization of the oxamato bridge, with accumulation of negative charges on both sides and a charge depletion on C1 and C2. The bridge is furthermore involved in two different bonding schemes with the Cu and Mn metals: significant covalent Cu-bridge interactions occur, the Cu−N bond being stronger than the Cu−O3 one, whereas the Mn−O bonds are of ionic character. The observed high conjugation and delocalization of the oxamato group explain the efficiency of the magnetic interactions even through extended bridges. According to the present study, strong intrachain magnetic couplings could be achieved by a careful choice of bridging ligands: the electron conjugation has to be enforced on the whole bridge, which is the case for oxalato, oxamido, oxamato, and so forth moiety; diffuse orbitals on the coordinating atoms allow strong metal−bridge interactions and therefore help spin delocalization from the metals to the bridge. Replacing all O atoms of an oxalato group by N atoms (or even better by S atoms) should therefore induce higher exchange *J* coupling.

A comparative and systematic ED study on other bridged Mn−Cu chain compounds (i.e., oxalato, oxamido, oxamato, thio-oxalato, and so forth) could lead to a better understanding of the superexchange interaction mechanisms with a topological classification of the interactions.

Supporting Information Available: Laplacian maps in the Cu−O3−O5 and Mn−O1−O4 (b) planes, gradient maps in hydrogen bond regions and all multipolar model parameters are available as Supporting Information. This material is available free of charge via the Internet at http://pubs.acs.org.

JA030279U

(65) Verdaguer, M.; Kahn, O.; Julve, M.; Gleizes, A. *New J. Chem.* **1985**, *9(5)*, 325.
(66) McConnell, H. M. *J. Phys. Chem.* **1963**, *39*, 1910.
(67) Johnson, C. K. *ORTEP II*; Report ORNL-5738; Oak Ridge National Laboratory: Tennessee, USA, 1976.